

PA-MIL: Phenotype-Aware Multiple Instance Learning Guided by Language Prompting and Genotype-to-Phenotype Relationships

Zekang Yang¹ Hong Liu^{1*} Xiangdong Wang¹

¹ Institute of Computing Technology, Chinese Academy of Sciences

Abstract

Deep learning has been extensively researched in the analysis of pathology whole-slide images (WSIs). However, most existing methods are limited to providing prediction interpretability by locating the model’s salient areas in a post-hoc manner, failing to offer more reliable and accountable explanations. In this work, we propose *Phenotype-Aware Multiple Instance Learning (PA-MIL)*, a novel ante-hoc interpretable framework that identifies cancer-related phenotypes from WSIs and utilizes them for cancer subtyping. To facilitate PA-MIL in learning phenotype-aware features, we 1) construct a phenotype knowledge base containing cancer-related phenotypes and their associated genotypes. 2) utilize the morphological descriptions of phenotypes as language prompting to aggregate phenotype-related features. 3) devise the *Genotype-to-Phenotype Neural Network (GP-NN)* grounded in genotype-to-phenotype relationships, which provides multi-level guidance for PA-MIL. Experimental results on multiple datasets demonstrate that PA-MIL achieves competitive performance compared to existing MIL methods while offering improved interpretability. PA-MIL leverages phenotype saliency as evidence and, using a linear classifier, achieves competitive results compared to state-of-the-art methods. Additionally, we thoroughly analyze the genotype-phenotype relationships, as well as cohort-level and case-level interpretability, demonstrating the reliability and accountability of PA-MIL. The code is available at <https://github.com/yangze-kang/PA-MIL>

1. Introduction

Deep learning technology has demonstrated outstanding performance in the automatic analysis of pathology whole slide images (WSIs), significantly advancing Computational Pathology (CPath) and cancer-assisted diagnosis [3, 6, 23, 25, 32, 42]. Although deep neural network models can achieve excellent performance, their black-box nature

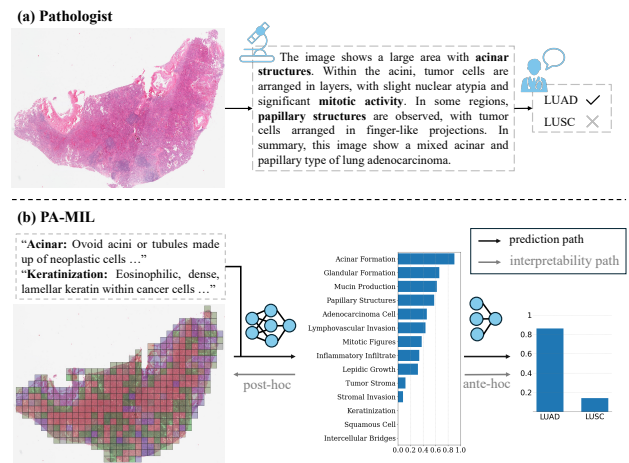


Figure 1. Comparison of the diagnostic process. (a) The diagnostic process of pathologists. (b) The predictive pathway and diagnostic evidence of PA-MIL.

makes it difficult to provide reasonable interpretability for their predictions. However, in real clinical contexts, a reliable and accountable AI algorithm is extremely important. It should provide more detailed evidence to support its predictions in order to gain the trust of users (or pathologists). Previous post-hoc interpretability methods [5, 15, 25, 35] are limited to locating salient regions without providing more detailed or convincing diagnostic evidence. In practice, as shown in Figure 1a, pathologists analyze WSIs by observing cell morphology and tissue structures to identify the clinical saliency of specific phenotypes (e.g., glandular structures, keratinization, intercellular bridges). They then make diagnoses based on the correlation between these phenotypes and cancer subtypes. It naturally raises the question: *Can a deep neural network model act like pathologists, identifying cancer phenotypes from WSIs and making diagnoses based on them?*

There are two main challenges that hinder the emergence of such a model. (1) *Which phenotypes to recognize from pathological images?* (2) *How can neural network models learn phenotype-related features from WSIs without phenotype annotations?* To address these challenges, we first

*Corresponding author: hliu@ict.ac.cn

build a phenotypic knowledge base by leveraging GPT-4 and the expertise of pathologists. Subsequently, we introduce textual descriptions of phenotypes and transcriptomics data paired with WSIs to assist in learning cancer phenotype features from WSIs. Due to the superpixel nature of pathology images, they are often divided into patches for processing. In recent years, pathology-specific CLIP models [13, 26, 37, 49] have demonstrated exceptional performance in tasks such as text-to-image retrieval. Such CLIP models can be used to roughly identify patches related to specific phenotypes from the large number of patches in each WSI, based on language prompting of the phenotypes. Compared to a single subtype label, the transcriptomic data offer a much richer and more detailed molecular profile. Furthermore, there are close relationships between genotypes and phenotypes, as gene expression at the microscopic level determines the macroscopically visible phenotypes [7, 19]. Based on the genotype-to-phenotype relationships, finer-grained genotype-specific information can be provided to the neural network models to help them recognize phenotypes from histological images.

Based on these insights, we propose a phenotype-aware multiple instance learning model (PA-MIL) that can identify phenotypes from WSIs and make diagnoses based on them. PA-MIL first utilizes a text encoder and an image encoder to extract textual features of phenotype descriptions and image features of WSIs, respectively. It then utilizes the cross-attention between the textual features and patch features to obtain phenotype features. Next, the clinical saliency of each phenotype is predicted based on its features, and finally, cancer diagnosis is performed based on the clinical saliency of the phenotypes. To facilitate model training, we also devise a genotype-to-phenotype neural network model (GP-NN) based on transcriptomic data and the relationship between genotypes and phenotypes as the teacher model. GP-NN shares a similar design with PA-MIL. It first divides the transcriptomic data into different groups based on their associations with various phenotypes. Then, different MLPs are used to learn the interactions between genes within each group, generating corresponding genotype-to-phenotype features. These features are then used to predict the clinical saliency of the associated phenotypes. Finally, the cancer diagnosis is made based on the clinical saliency of each phenotype. Due to the similar design of GP-NN and PA-MIL, GP-NN can provide PA-MIL with multi-hierarchical supervisory information, including phenotype feature level and phenotype saliency level. This helps PA-MIL learn more precise phenotype-related information during the training phase. The contributions of this work are summarized as follows:

- We construct a phenotype knowledge base that includes cancer-related phenotypes observable in WSIs. Each phenotype contains its morphological description and the as-

sociated gene set.

- We propose a phenotype-aware multiple instance learning method (PA-MIL), the first method that explicitly identifies the cancer-related phenotypes from WSIs and uses phenotypic evidence for diagnosis prediction.
- We propose a phenotype learning approach that leverages language prompts and genotype-to-phenotype relationships to guide PA-MIL in extracting discriminative phenotypic features from WSIs.
- We conduct comprehensive experiments and interpretability analyses, demonstrating that PA-MIL can achieve competitive performance compared to previous MIL methods and provide more clinically valuable phenotype-based evidence for its predictions.

2. Related Work

2.1. Multiple Instance Learning

Early methods for pathological image analysis primarily relied on pathologists manually annotating regions of interest [28, 40, 44, 52]. Subsequent research introduced multiple instance learning techniques, enabling the direct analysis of entire pathological images [6, 14, 22, 32, 43]. Existing MIL methods can be categorized into two groups based on the following principles: the instances within a bag are independent, or the instances within a bag are interdependent. The former primarily focuses on identifying key instances from a large number of patches in a whole slide image (WSI) [1, 14, 30, 34]. The latter mainly emphasizes learning the relationships between instances using methods such as prototype learning [35, 39, 46, 47], graph neural networks [2, 4, 10, 12], and self-attention mechanisms [8, 22, 24, 32]. PA-MIL is somewhat similar to prototype-based MIL methods, as both leverage the distribution of different phenotypes or prototypes within a specific WSI as the basis for diagnosis. However, prototypes are typically obtained through global clustering and lack explicit semantic meaning. While post-hoc analysis can reveal that some prototypes contain specific phenotype patterns, they still lack stronger reliability and interpretability. In contrast, cancer-related phenotypes are directly extracted from WSIs based on histopathological knowledge, providing clear semantic meaning and stronger interpretability.

2.2. Interpretability Methods

Methods based on hand-crafted features [11, 18, 48] first extract properties related to the morphology and spatial distribution of cells in WSIs. These features are then used for diagnostic predictions, offering good interpretability. Deep learning-based methods demonstrate superior performance but lack interpretability, relying on contributions of attention [14, 32] or gradient [31, 51] to identify salient regions of WSI. Such post-hoc methods merely highlight

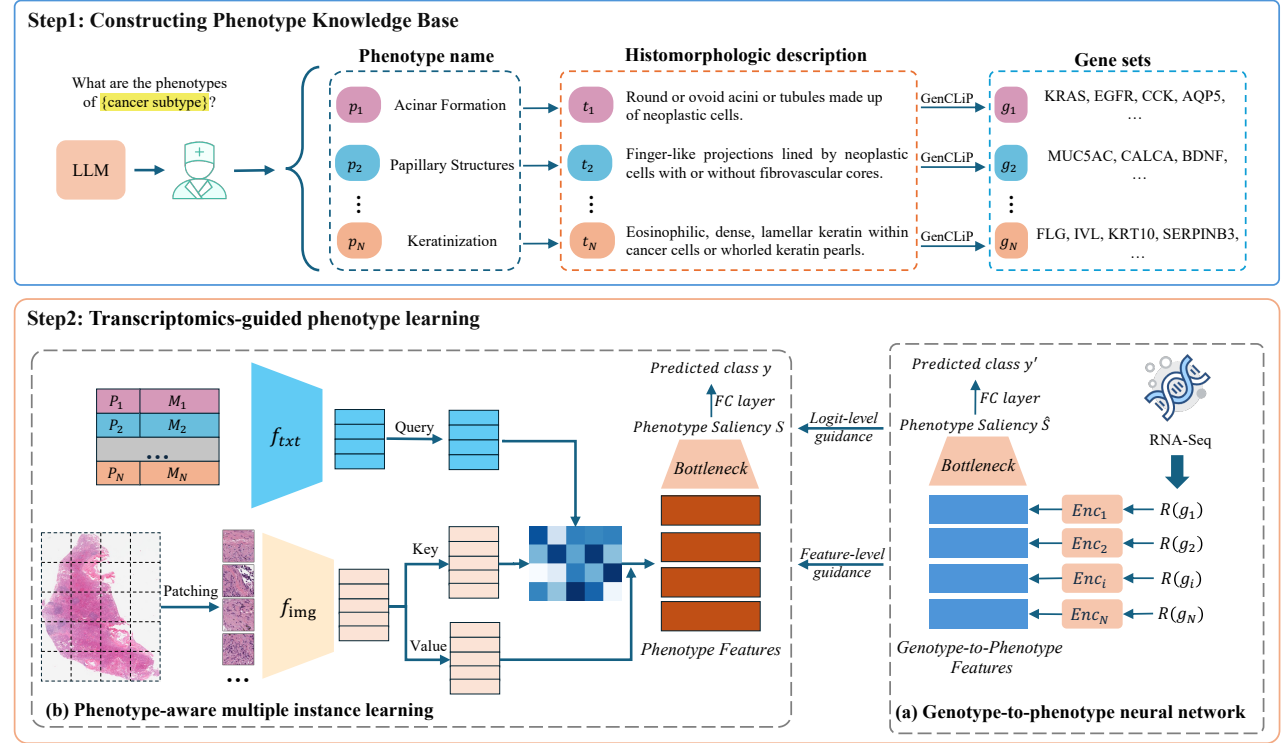


Figure 2. Overview of proposed PA-MIL and training method. **Step 1:** Constructing phenotypic knowledge base. **Step 2a:** Training genotype-to-phenotype neural network. **Step 2b:** Training phenotype-aware multiple instance learning with transcriptomic guidance.

superficial associations between inputs and outputs, without offering deeper or more convincing evidence for predictions. SI-MIL [17] compromises between model performance and interpretability by identifying salient regions through post-hoc methods and using hand-crafted features from these regions for diagnostic predictions. Our goal is to design a self-interpretability deep neural network model that is capable of identifying cancer-related phenotypes and making diagnoses based on these phenotypes. In the domain of natural images, the Concept Bottleneck Models (CBMs) [21] identify human-understandable concepts from the input and make predictions based on these interpretable concepts, providing strong interpretability for the final prediction. However, CBMs are limited by their reliance on concept-annotated data and a compromise in performance. In this paper, we introduce language prompting and genomic data to address these limitations.

3. Method

In this section, we present the architecture and training methods of Phenotype-Aware Multiple Instance Learning (PA-MIL) in detail (overview Figure 2). We first construct a phenotypic knowledge base containing cancer-related phenotypes and their associated genotypes (Sec. 3.1). Next, we provide a detailed explanation of the proposed PA-MIL

(Sec. 3.2). Based on the relationships between phenotypes and genotypes, we devise a genotype-to-phenotype neural network (GP-NN) using transcriptomic data (Sec. 3.3). Finally, we introduce a method to use transcriptome information to guide PA-MIL to learn cancer-related phenotypes from WSIs. (Sec. 3.4).

3.1. Phenotype Knowledge Base

First, we construct a phenotype knowledge base \mathcal{K} to provide medical prior knowledge to support our method. Each phenotype in \mathcal{K} has its corresponding histomorphological description and function-related gene set. In this section, we provide a detailed description of the process of constructing the phenotype knowledge base. **Identifying cancer-related phenotypes:** Large language models (LLMs) possess a vast amount of knowledge. We prompt LLMs to generate potential phenotypes associated with specific cancers, which are then refined and validated through expert correction. As a result, we identify N phenotypes $\mathcal{P} = \{p_1, p_2, \dots, p_N\}$ related to the specific cancer c . **Generating histomorphological-related descriptions:** In a similar manner, we design prompts for LLMs to describe the morphological structures of each phenotype and manually correct their outputs, resulting in the histomorphological descriptions $\mathcal{T} = \{t_1, t_2, \dots, t_N\}$ for all phenotypes. **Retrieving**

ing function-related gene sets: GenCLiP [41] is a tool that provides rapid retrieval of function-related genes according to custom terms from the entire PubMed database. We use the names and synonyms of the phenotypes as queries for GenCLiP and obtain the gene sets $\mathcal{G} = \{g_1, g_2, \dots, g_N\}$ associated with the phenotypes. Then we have the phenotype knowledge base $\mathcal{K} = \{(p_i, t_i, g_i) | i \in I, p_i \in \mathcal{P}, t_i \in \mathcal{T}, g_i \in \mathcal{G}\}$.

3.2. Phenotype-Aware Multiple Instance Learning

Multiple Instance Learning (MIL). MIL is a weakly-supervised learning framework designed for handling data with a set-based structure. When applying MIL to computational pathology, a given WSI X^j is segmented into multiple fixed-size patches $X^j = \{x_i^j\}_{i=1}^{M_j}$, and a pre-trained feature extractor f_{img} is used to extract features $H^j = f_{img}(X^j)$ from these patches. Where M_j denotes the number of patches extracted from X^j . The set of features $H^j \in \mathbb{R}^{M_j \times d}$ is aggregated to obtain a WSI-level feature $h_w^j \in \mathbb{R}^d$. And h_w^j is then applied to prediction tasks.

The PA-MIL we propose aims to learn a WSI-level feature $S^j = \{s_i^j\}_{i=1}^N$ with $S^j \in \mathbb{R}^N$ that possesses inherent interpretability, where each element s_i^j corresponds to the saliency score of a cancer-related phenotype. And the diagnostic predictions are made based on S^j . In each inference, PA-MIL takes the names \mathcal{P} and histomorphological descriptions \mathcal{T} of phenotypes and the features H^j of WSI X^j as input. **Encoding language prompting:** We use a weight-frozen text feature extractor f_{txt} to extract the textual features $U = \{u_i\}_{i=1}^N$ with $u_i \in \mathbb{R}^d$ for all phenotypes:

$$u_i = f_{txt}([p_i, t_i]); \quad i \in \{1, 2, \dots, N\} \quad (1)$$

Extracting phenotype-related features: Considering that pretrained vision-language models have limited ability to recognize cancer-related phenotypes [36], we design a learnable cross-attention method to fine-tune it and extract phenotype-related features $V^j \in \mathbb{R}^{N \times d}$ from WSI:

$$\begin{aligned} V^j &= f_p(H^j, U) \\ &= A^j \times W_v^T(H^j) \\ &= \text{softmax}\left(\frac{W_q(U)W_k^T(H^j)}{\sqrt{d}}\right)W_v^T(H^j) \end{aligned} \quad (2)$$

Where $W_q(\cdot)$, $W_k(\cdot)$ and $W_v(\cdot)$ are learnable linear projections. $A^j \in \mathbb{R}^{N \times M_j}$ represents the contribution of each patch in X^j to different phenotypes. **Aligning cohort-level phenotype features:** PA-MIL aims to extract mutually independent phenotypic features. Accordingly, features representing the same phenotype across different samples within a cohort should be close in the feature space, while features of different phenotypes should be well separated. Assuming the cluster centers of phenotypes are represented

by $\bar{V} \in \mathbb{R}^{N_c \times d}$. For the phenotype feature V_i^j , it has the positive sample \bar{V}_i and negative samples $\{\bar{V}_k\}_{k \neq i}^N$. Then we have the objective function:

$$L_{contrast} = \frac{1}{N} \sum_{k=1}^N \log\left(\frac{\exp(V_k^j \bar{V}_k^T / \tau)}{\sum_{k'}^N \exp(V_k^j \bar{V}_{k'}^T / \tau)}\right) \quad (3)$$

Due to the superpixels of WSIs, it is difficult to compute \bar{V} by using a large batch size. We draw on the previous contrastive learning method based on self-distillation and use the momentum update strategy to obtain the cluster centers:

$$\bar{V} = \alpha \bar{V} + (1 - \alpha) V^j \quad (4)$$

where α denotes the momentum value. **Predicting saliency scores of phenotypes:** To facilitate better interpretability, we introduce a bottleneck [21] layer $W_w(\cdot)$ to predict the saliency scores of the phenotypes. To mitigate the leakage of subtype label information into phenotypic prediction, we employ a layer normalization (LN) layer as the activation function to compute relative saliency scores, which are then used as the final saliency scores $S^j = \text{LN}(W_w(V^j))$.

Classifying cancer subtype: Histomorphological phenotypes are important evidence for cancer diagnosis and subtype classification. We use the saliency scores of phenotypes as the input features for the classifier $f_a(\cdot)$ to predict cancer subtypes y_w^j and use the cross-entropy loss function $L_{ce} = y_t^j \log(y_w^j)$ as the objective function for end-to-end training, where y_t^j is the label of the j -th sample.

3.3. Genotype-to-Phenotype Neural Network

Phenotypes are potentially associated with specific gene sets, and the phenotypes observed in histopathological images are typically the macroscopic results of specific gene expressions at the microscopic level [50]. Transcript abundance (RNA-Seq) reflects gene expression levels. Therefore, we devise the genotype-to-phenotype neural network (GP-NN) to learn phenotype-related information from transcriptomics data. **Encoding phenotype-related features:** We first divide all the RNA-Seq abundance R^j into different sets $\{R^j(g_1), R^j(g_2), \dots, R^j(g_N)\}$ based on the relationship between genotype and phenotype, where j denotes the j -th sample. RNA-Seq abundance is typically quantified as an 1×1 attribute. We can employ a set of multi-layer perceptions (MLPs) $\{Enc_1, Enc_2, \dots, Enc_N\}$ to encode the interactions between genes within different gene sets that contribute to the corresponding phenotypes, thereby obtaining phenotype-related features $Z^j \in \mathbb{R}^{N \times d}$:

$$z_i^j = Enc_i(R^j(g_i)); \quad i \in \{1, 2, \dots, N\} \quad (5)$$

Predicting the saliency scores of phenotypes: Similar to PA-MIL, we also employ a bottleneck layer $W_g(\cdot)$ followed by a LN layer to predict the saliency scores $\hat{S}^j \in \mathbb{R}^N$ of

the phenotypes: $\hat{S}^j = \text{LN}(W_g(Z^j))$. **Cancer subtyping:** Finally, the scores \hat{S}^j are fed into the classifier $f_b(\cdot)$ to predict cancer subtypes $\hat{y}_g^j = f_b(\hat{S}^j)$, thereby supervising the training of the GP-NN.

3.4. Transcriptomics-Guided Phenotype Learning

To facilitate PA-MIL in learning phenotype-related information, we propose a transcriptomics-guided phenotype learning method. In the following content, we provide a detailed introduction to the design of the guidance methods and learning methods.

Guidance method. We utilize the weight-frozen GP-NN to provide both logit-level and feature-level guidance for PA-MIL, enhancing its interpretability while achieving competitive performance on downstream tasks. **Logit-level:** Minimize the distance L_{logit} between the phenotype saliency scores predicted by PA-MIL and GP-NN. **Feature-level:** Minimize the distance L_{feat} between the phenotype-related features extracted by PA-MIL and GP-NN. We use L2 distance as the distance metric function:

$$L_{logit} = \frac{1}{N} \|S^j - \hat{S}^j\|_2^2; \quad (6)$$

$$L_{feat} = \frac{1}{N} \sum_{i=1}^N \frac{1}{d} \|v_i^j - z_i^j\|_2^2 \quad (7)$$

Learning method. We systematically study two training methods. **Sequential training:** PA-MIL first learns to extract phenotype-related features and predict phenotype saliency scores: $\hat{f}_p, \hat{W}_w = \arg \min_{f_p, W_w} \sum_j (L_{feat} + L_{logit} + L_{contrast})$. Subsequently, with the weights of f_p and W_w frozen, PA-MIL learns to predict cancer subtypes based on the phenotype saliency scores: $\hat{f}_a = \arg \min_{f_a} \sum_j L_{ce}$. **Joint training:** Treat phenotype learning as an auxiliary branch to enable simultaneous learning of subtype classification and phenotype prediction: $\hat{f}_a, \hat{f}_p, \hat{W}_w = \arg \min_{f_a, f_p, W_w} \sum_j [L_{ce} + L_{contrast} + \lambda (L_{feat} + L_{logit})]$, where λ denotes the weight for phenotype learning supervision.

4. Experiment and Results

4.1. Dataset and Implementation Details

Datasets. We evaluate PA-MIL on two different subtyping tasks and four different WSI datasets: Non-Small Cell Lung Carcinoma (NSCLC) subtyping on TCGA (2 classes) and CPTAC (2 classes). Renal Cell Carcinoma (RCC) subtyping on TCGA (3 classes) and CPTAC (2 classes). We train the models using datasets from the TCGA and then test them on datasets from both the TCGA and CPTAC. For TCGA, we perform 5-fold cross-validation to conduct five repeated experiments. The datasets from CPTAC were used as an external dataset to validate the model’s generalizability. We

use the accuracy and area under the curve (AUC) metrics for evaluation on NSCLC subtyping and balanced accuracy and weighted F1 as evaluation metrics for RCC subtyping due to the imbalance among subtypes.

Implementation. We follow the CLAM [25] to preprocess the WSIs. We first employ OTSU’s threshold method to segment the tissue regions in the WSIs at low magnification. Then we divide the WSIs at 20x magnification into non-overlapping patches of size 512×512 pixels, which are subsequently resized to 448×448 pixels before feature extraction. We set the momentum value α at 0.9. All the comparison models except SI-MIL [17] utilize the image encoder of CONCH [26] to extract the patch features. We also use the text encoder of CONCH to extract the textual features of the phenotypes. All models are trained for 20 epochs using the Adam optimizer [20], with a batch size of 1 and a gradient accumulation step of 32. The learning rate is set to 5×10^{-4} , the weight decay to 1×10^{-4} , and the gradient clipping threshold to 10.

4.2. Comparisons with State-of-the-Art

Baselines. We compare our method with both post-hoc methods and ante-hoc methods. AMIL [14], Trans-MIL [32], DSMIL [22], and AttMISL [45] lack intrinsic interpretability and can only be explained through post-hoc methods. AdditiveMIL [16], SI-MIL [17], and Panther [35] optimize the network design in an effort to provide ante-hoc explanations for the model’s predictions. AMIL is used as the base model for AdditiveMIL. SI-MIL does not provide the complete hand-crafted features, and we directly report the results from their paper. Panther+lin. and Panther+MLP predict based on prototype-related features, using a linear classifier and a multilayer perceptron, respectively.

Results. Table 1 presents the result. PA-MIL_S and PA-MIL_J represent the models obtained through sequential learning and joint learning, respectively. “Feature” refers to using a transformer for prediction based on phenotypic features. “Score” represents using a linear classifier for prediction based on phenotypic saliency scores. * are obtained from their papers, and other results are re-implemented with the same image encoder. Overall, both PA-MIL_S and PA-MIL_J consistently outperform or are on par with all post-hoc and ante-hoc baselines.

Phenotypic features vs. phenotypic saliency scores

Due to the bottleneck layer, a saliency score loses more information compared to a feature vector. Additionally, the linear classifier can learn fewer patterns compared to the nonlinear classifier. However, subtyping with phenotypic saliency scores has achieved performance that is comparable to, or even better than, phenotypic features. It suggests that the phenotypic saliency scores predicted by PA-MIL is directly associated with cancer subtypes, and excellent results can be achieved with a simple linear classifier. In

Table 1. Results of PA-MIL and baselines on four different datasets. All methods except * use CONCH [26] to extract path features. \diamond denotes post-hoc methods and \heartsuit denotes ante-hoc methods. The mean and standard deviation of the five-fold cross-validation are reported. Best performance in **bold**, second best underlined.

Train on	TCGA-NSCLC				TCGA-RCC			
	TCGA		CPTAC		TCGA		CPTAC	
Test on	Acc.	AUC	Acc.	AUC	Bal. acc.	F1	Bal. acc.	F1
\diamond AMIL [14]	94.19 \pm 1.64	98.01 \pm 0.98	91.98 \pm 0.56	97.60 \pm 0.27	94.24 \pm 4.25	<u>95.77\pm1.87</u>	80.57 \pm 1.59	92.62 \pm 0.56
\diamond TransMIL [32]	93.60 \pm 1.28	97.09 \pm 2.71	91.17 \pm 0.74	96.60 \pm 0.65	93.62 \pm 2.64	95.19 \pm 0.87	83.92 \pm 5.32	91.20 \pm 1.26
\diamond DSMIL [22]	93.62 \pm 1.34	97.94 \pm 1.19	91.60 \pm 0.43	97.46 \pm 0.05	93.92 \pm 1.93	94.68 \pm 0.56	82.19 \pm 0.77	94.01 \pm 0.37
\diamond AttMISL [45]	92.93 \pm 1.11	97.82 \pm 0.93	91.34 \pm 0.24	97.48 \pm 0.13	94.44 \pm 1.70	95.58 \pm 1.38	80.51 \pm 2.27	91.77 \pm 0.82
\heartsuit AdditiveMIL [16]	94.09 \pm 1.72	98.02 \pm 1.08	91.92 \pm 0.64	97.41 \pm 0.29	95.42 \pm 1.51	95.68 \pm 0.70	81.86 \pm 1.21	92.76 \pm 0.66
\heartsuit SI-MIL* [17]	88.4	94.1	-	-	-	-	-	-
\heartsuit Panther+lin. [35]	92.27 \pm 2.68	96.92 \pm 1.36	89.90 \pm 0.66	96.87 \pm 0.30	90.34 \pm 5.31	94.41 \pm 0.91	75.60 \pm 1.35	92.27 \pm 0.63
\heartsuit Panther+MLP [35]	92.85 \pm 2.15	97.25 \pm 1.37	90.51 \pm 1.13	97.20 \pm 0.29	91.05 \pm 3.94	93.92 \pm 1.21	78.88 \pm 3.28	92.33 \pm 0.80
\heartsuit PA-MIL _S (feature)	94.77\pm1.56	97.80 \pm 0.91	92.39 \pm 0.18	97.77 \pm 0.15	94.52 \pm 1.78	95.26 \pm 0.71	84.36 \pm 3.14	92.97 \pm 1.58
\heartsuit PA-MIL _J (feature)	94.09 \pm 1.71	98.17 \pm 0.99	92.96\pm0.48	97.95\pm0.11	96.00\pm0.88	95.63\pm0.85	82.22 \pm 1.31	94.06 \pm 0.48
\heartsuit PA-MIL _S (score)	94.19 \pm 1.71	98.07 \pm 0.84	92.71 \pm 0.46	97.75 \pm 0.20	93.03 \pm 3.84	94.52 \pm 0.75	84.90\pm1.93	94.50\pm0.78
\heartsuit PA-MIL _J (score)	94.68 \pm 1.30	98.42\pm0.84	92.62 \pm 0.80	97.69 \pm 0.50	95.66 \pm 1.86	95.69 \pm 0.59	82.58 \pm 0.85	93.34 \pm 1.01

contrast, Panther+MLP outperforms Panther+lin, suggesting that prototypes obtained through clustering may not be directly related to the subtype classification.

Table 2. Ablation of modules. ‘LP’ means language prompting. ‘PA’ means cohort-level phenotypic features alignment. ‘TG’ means transcriptomics guidance.

Module	TCGA		CPTAC	
	Acc	AUC	Acc	AUC
baseline	94.09	97.13	91.80	97.67
+LP	94.00	97.76	92.54	97.33
+LP+PA	93.70	97.89	92.17	97.42
+LP+PA+TG	94.68	98.42	92.62	97.69

Sequential Training vs. Joint Training When using phenotypic saliency scores for prediction, PA-MIL_J performs better on the in-domain test dataset, while PA-MIL_S shows better out-of-domain performance. This suggests that separately training the phenotypic saliency prediction and the subtype classification can help the model achieve better out-of-domain generalization performance.

4.3. Ablation Studies

Ablation of modules. We conducted ablation experiments on the different modules of PA-MIL, and the experimental results are presented in Table 2. We replace the cross-attention mechanism that leverages language prompting with a self-attention mechanism to learn phenotypic features, creating a baseline. Note that although baseline achieves good performance, it learns phenotype-agnostic features. As shown in the table, language prompting, phenotypic feature alignment, and transcriptomic guidance each contribute to improving the model’s performance.

Table 3. Ablation study of the guidance method, evaluated using mean accuracy and mean AUC across 5-fold on the NSCLC task. ‘Feat’ represent feature-level guidance, and ‘Logit’ means logit-level guidance.

Feat	Logit	TCGA		CPTAC	
		Acc	AUC	Acc	AUC
		93.70	97.89	92.17	97.42
✓		94.67	97.90	92.53	97.59
	✓	94.49	97.90	92.30	97.24
✓	✓	94.68	98.42	92.62	97.69

Table 4. Ablation study of the objective functions (Obj.), evaluated using mean accuracy and mean AUC across 5-fold on the NSCLC.

Obj.	TCGA		CPTAC	
	Acc	AUC	Acc	AUC
CL	93.52	97.84	91.38	97.31
L1	94.68	97.98	92.14	97.64
L2	94.68	98.42	92.62	97.69

Effect of guidance methods. Table 3 presents the effect of different levels of guidance when training PA-MIL with transcriptomic supervision. The best performance is achieved by combining both feature-level and logit-level guidance, indicating that multi-hierarchical supervision can effectively enhance PA-MIL’s learning. **Effect of objective function.** To facilitate PA-MIL learning knowledge from the transcriptomic data, we compared three objective functions: contrastive learning (CL) [38], L1 distance, and L2 distance. Table 4 illustrates that L2 distance exhibits the best performance.

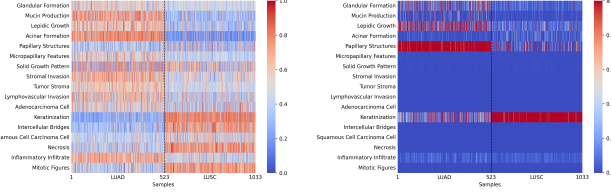


Figure 3. Heatmaps of phenotypic saliency scores under different activation functions. **(Left:** Layer normalization, **Right:** LeakyReLU) The heatmap illustrates the saliency scores of various phenotypes across 1372 samples from the CPTAC-NSCLC. Samples 1-683 are lung adenocarcinoma, and samples 684-1372 are lung squamous cell carcinoma. A higher value indicates a greater saliency score.

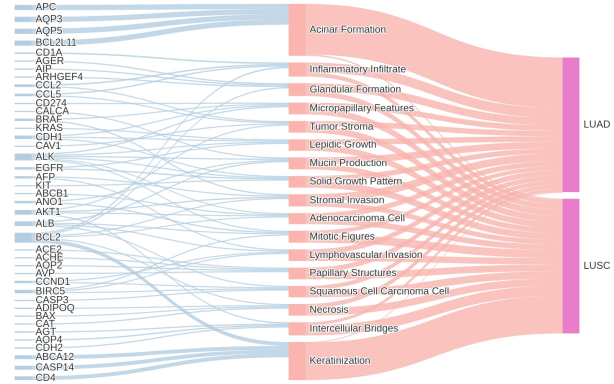


Figure 4. Relationships among genotypes, phenotypes, and cancer subtypes. Thicker lines means greater contributions. The top-4 genes contributing to each phenotype are shown.

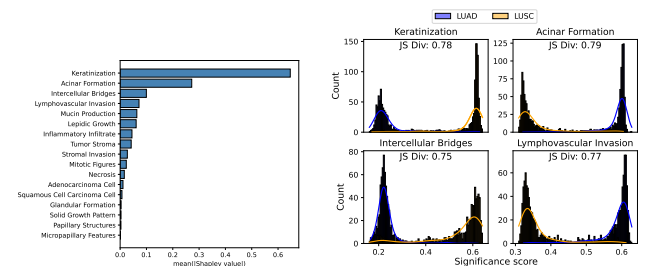
Ablation of activation functions for phenotype saliency scores. PA-MIL adopts an architecture similar to Concept Bottleneck Models (CBMs) [21], which are known to suffer from information leakage [27]. To mitigate this issue, our method designs the phenotype saliency score not as a direct indicator of phenotype presence but as a normalized measure of relative phenotype importance within each sample. Specifically, layer normalization ensures that the mean and variance of saliency activations are standardized, redistributing any class-specific signals that might leak into a particular phenotype channel across all phenotypes. This activation function reduces the overall impact of the information leakage. Figure 3 illustrate the phenotype saliency scores on the test dataset under different activation functions. As shown, using LeakyReLU leads to significant information leakage, with class signals primarily leaking into “Papillary Structures” and “Keratinization.” In contrast, when layer normalization is applied, the saliency maps exhibit no observable leakage, confirming its effectiveness.

5. Interpretability Analysis

5.1. Genotype-to-Phenotype Relationships

In this section, we explore the interpretative analysis of the genotype-to-phenotype neural network to investigate the relationship between genotype and phenotype, as well as the relationship between phenotype and cancer subtype diagnosis. Shapley values [33] measure the marginal contribution of different input features to the prediction of a model.

We use Shapley values to measure the contribution of gene expression levels to phenotypic saliency scores, as well as the contribution of phenotypic saliency scores to cancer subtype. The visualization results are shown in Figure 4. For example, the APC gene plays a crucial role in acinar formation. Studies [9] have shown that underexpression of APC leads to abnormal accumulation of β -catenin, which, via the Wnt signaling pathway, regulates cell proliferation and differentiation, ultimately contributing to the de-



(a) Ranking of phenotypic contributions to subtyping. (b) The saliency scores distribution of the top-4 contributing phenotypes.

Figure 5. Cohort interpretability analysis.

velopment of acinar cell carcinoma. This demonstrates that by analyzing the GP-NN network, it is possible to explore the relationship between genotype and phenotype and generate new biological insights. As shown in Figure 4, acinar formation and micropapillary structures contribute significantly to lung adenocarcinoma, while keratinization and intercellular bridges contribute significantly to lung squamous cell carcinoma. These findings are consistent with the corresponding medical knowledge [29]: acinar formation, micropapillary structures, and keratinization are characteristic of the respective histological subtypes of lung adenocarcinoma and lung squamous cell carcinoma, while intercellular bridges are more prominent in squamous epithelium.

5.2. Cohort Interpretability

There are often common and specific patterns within a cohort and across cohorts. We use the results of PA-MIL on the CPTAC-NSCLC to perform interpretability analysis from a cohort perspective. Figure 5a illustrates that keratinization and acinar formation are the most salient features for distinguishing lung adenocarcinoma from lung squamous cell carcinoma. It can be observed that “keratinization” and “acinar formation” make the most significant con-

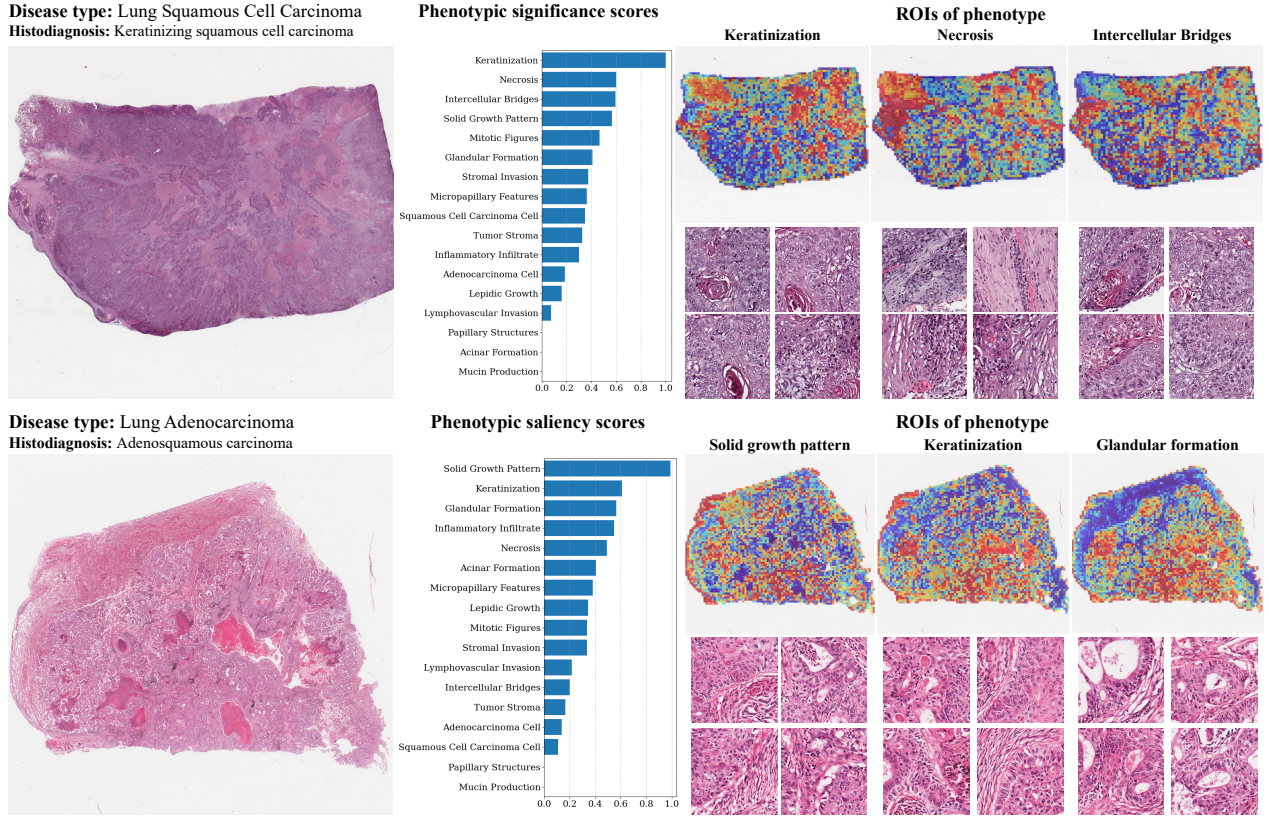


Figure 6. Case interpretability analysis. Every sample shows the prediction of phenotypic saliency scores, the heatmaps of the regions of interest for the top-3 contributing phenotypes, and representative patch images. **Top:** Keratinizing squamous cell carcinoma sample. **Bottom:** Adenosquamous carcinoma sample.

tributions to the subtyping of lung adenocarcinoma and lung squamous cell carcinoma. Figure 5b shows the saliency distribution of the top-4 contributing phenotypes. We also use Jensen-Shannon (JS) divergence to measure the distance between the two distributions. All four phenotypes exhibit high JS divergence values, indicating these phenotypes can effectively distinguish different subtypes.

5.3. Case Interpretability

We conduct a detailed analysis of the prediction results on the test samples from the perspective of individual case predictions. Figure 6 presents the prediction result for two samples. It can be observed that for the sample histologically diagnosed as keratinized-type lung squamous cell carcinoma, PA-MIL accurately predicted keratinization as the most prominent phenotype and successfully localized the corresponding regions of interest. In contrast, for the sample histologically diagnosed as acinar-type lung adenocarcinoma, PA-MIL can successfully predict that its most prominent phenotype is acinar formation and identify the corresponding regions of interest. In practice, there are some adenosquamous carcinoma samples that contain both lung adenocarcinoma and lung squamous cell carcinoma. These

samples are incorrectly labeled as lung adenocarcinoma or lung squamous cell carcinoma, making it challenging for single-label classification models trained on such data to recognize these complex patterns. The bottom panel of Figure 6 illustrates such a sample. As shown in the figure, in the top-3 contributing phenotypes predicted by PA-MIL, features of squamous cell carcinoma, such as keratinization, and features of lung adenocarcinoma, such as glandular formation, are both present. This suggests that the phenotypes identified by PA-MIL can serve as evidence to recognize such complex patterns.

6. Conclusion

We present PA-MIL, a novel ante-hoc interpretable method for cancer subtyping. PA-MIL identifies the saliency of cancer-related phenotypes from pathology images and subsequently performs cancer subtype diagnosis, providing reliable phenotypic evidence for diagnostic predictions. Extensive experiments and interpretability analyses demonstrate the performance and reliability of PA-MIL. Future work will explore learning more diverse phenotypes for application in various downstream tasks.

References

[1] Gabriele Campanella, Matthew G Hanna, Luke Geneslaw, Allen Miraflor, Vitor Werneck Krauss Silva, Klaus J Busam, Edi Brogi, Victor E Reuter, David S Klimstra, and Thomas J Fuchs. Clinical-grade computational pathology using weakly supervised deep learning on whole slide images. *Nature medicine*, 25(8):1301–1309, 2019. [2](#)

[2] Tsai Hor Chan, Fernando Julio Cendra, Lan Ma, Guosheng Yin, and Lequan Yu. Histopathology whole slide image analysis with heterogeneous graph representation learning. In *Proceedings of the IEEE/CVF Conference on Computer Vision and Pattern Recognition*, pages 15661–15670, 2023. [2](#)

[3] Pingyi Chen, Honglin Li, Chenglu Zhu, Sunyi Zheng, Zhongyi Shui, and Lin Yang. Wsicaption: Multiple instance generation of pathology reports for gigapixel whole-slide images. In *International Conference on Medical Image Computing and Computer-Assisted Intervention*, pages 546–556. Springer, 2024. [1](#)

[4] Richard J Chen, Ming Y Lu, Muhammad Shaban, Chengkuan Chen, Tiffany Y Chen, Drew FK Williamson, and Faisal Mahmood. Whole slide images are 2d point clouds: Context-aware survival prediction using patch-based graph convolutional networks. In *Medical Image Computing and Computer Assisted Intervention–MICCAI 2021: 24th International Conference, Strasbourg, France, September 27–October 1, 2021, Proceedings, Part VIII 24*, pages 339–349. Springer, 2021. [2](#)

[5] Richard J Chen, Chengkuan Chen, Yicong Li, Tiffany Y Chen, Andrew D Trister, Rahul G Krishnan, and Faisal Mahmood. Scaling vision transformers to gigapixel images via hierarchical self-supervised learning. In *Proceedings of the IEEE/CVF Conference on Computer Vision and Pattern Recognition*, pages 16144–16155, 2022. [1](#)

[6] Richard J Chen, Ming Y Lu, Drew FK Williamson, Tiffany Y Chen, Jana Lipkova, Zahra Noor, Muhammad Shaban, Maha Shady, Mane Williams, Bumjin Joo, et al. Pan-cancer integrative histology-genomic analysis via multimodal deep learning. *Cancer Cell*, 40(8):865–878, 2022. [1, 2](#)

[7] Michael Costanzo, Elena Kuzmin, Jolanda van Leeuwen, Barbara Mair, Jason Moffat, Charles Boone, and Brenda Andrews. Global genetic networks and the genotype-to-phenotype relationship. *Cell*, 177(1):85–100, 2019. [2](#)

[8] Olga Fourkioti, Matt De Vries, Chen Jin, Daniel C Alexander, and Chris Bakal. Camil: Context-aware multiple instance learning for cancer detection and subtyping in whole slide images. *arXiv preprint arXiv:2305.05314*, 2023. [2](#)

[9] Daniela Furlan, Nora Sahnane, Barbara Bernasconi, Milo Frattini, Maria Grazia Tibiletti, Francesca Molinari, Alessandro Marando, Lizhi Zhang, Alessandro Vanoli, Selenia Casnedi, et al. Apc alterations are frequently involved in the pathogenesis of acinar cell carcinoma of the pancreas, mainly through gene loss and promoter hypermethylation. *Virchows Archiv*, 464:553–564, 2014. [7](#)

[10] Yonghang Guan, Jun Zhang, Kuan Tian, Sen Yang, Pei Dong, Jinxi Xiang, Wei Yang, Junzhou Huang, Yuyao Zhang, and Xiao Han. Node-aligned graph convolutional network for whole-slide image representation and classification. In *Proceedings of the IEEE/CVF Conference on Computer Vision and Pattern Recognition*, pages 18813–18823, 2022. [2](#)

[11] PW Hamilton, N Anderson, PH Bartels, and D Thompson. Expert system support using bayesian belief networks in the diagnosis of fine needle aspiration biopsy specimens of the breast. *Journal of clinical pathology*, 47(4):329–336, 1994. [2](#)

[12] Wentai Hou, Yan He, Bingjian Yao, Lequan Yu, Rongshan Yu, Feng Gao, and Liansheng Wang. Multi-scope analysis driven hierarchical graph transformer for whole slide image based cancer survival prediction. In *International Conference on Medical Image Computing and Computer-Assisted Intervention*, pages 745–754. Springer, 2023. [2](#)

[13] Zhi Huang, Federico Bianchi, Mert Yuksekgonul, Thomas J Montine, and James Zou. A visual–language foundation model for pathology image analysis using medical twitter. *Nature medicine*, 29(9):2307–2316, 2023. [2](#)

[14] Maximilian Ilse, Jakub Tomczak, and Max Welling. Attention-based deep multiple instance learning. In *International conference on machine learning*, pages 2127–2136. PMLR, 2018. [2, 5, 6](#)

[15] Guillaume Jaume, Anurag Vaidya, Richard J Chen, Drew FK Williamson, Paul Pu Liang, and Faisal Mahmood. Modeling dense multimodal interactions between biological pathways and histology for survival prediction. In *Proceedings of the IEEE/CVF Conference on Computer Vision and Pattern Recognition*, pages 11579–11590, 2024. [1](#)

[16] Syed Ashar Javed, Dinkar Juyal, Harshith Padigela, Amaro Taylor-Weiner, Limin Yu, and Aaditya Prakash. Additive mil: Intrinsically interpretable multiple instance learning for pathology. *Advances in Neural Information Processing Systems*, 35:20689–20702, 2022. [5, 6](#)

[17] Saarthak Kapse, Pushpak Pati, Srijan Das, Jingwei Zhang, Chao Chen, Maria Vakalopoulou, Joel Saltz, Dimitris Samaras, Rajarsi R Gupta, and Prateek Prasanna. Si-mil: Taming deep mil for self-interpretability in gigapixel histopathology. In *Proceedings of the IEEE/CVF Conference on Computer Vision and Pattern Recognition*, pages 11226–11237, 2024. [3, 5, 6](#)

[18] Stephen J Keenan, James Diamond, W Glenn McCluggage, Hoshang Bharucha, Deborah Thompson, Peter H Bartels, and Peter W Hamilton. An automated machine vision system for the histological grading of cervical intraepithelial neoplasia (cin). *The Journal of pathology*, 192(3):351–362, 2000. [2](#)

[19] Yoo-Ah Kim, Dong-Yeon Cho, and Teresa M Przytycka. Understanding genotype-phenotype effects in cancer via network approaches. *PLoS computational biology*, 12(3):e1004747, 2016. [2](#)

[20] Diederik P Kingma. Adam: A method for stochastic optimization. *arXiv preprint arXiv:1412.6980*, 2014. [5](#)

[21] Pang Wei Koh, Thao Nguyen, Yew Siang Tang, Stephen Mussmann, Emma Pierson, Been Kim, and Percy Liang. Concept bottleneck models. In *International conference on machine learning*, pages 5338–5348. PMLR, 2020. [3, 4, 7](#)

[22] Bin Li, Yin Li, and Kevin W Eliceiri. Dual-stream multiple instance learning network for whole slide image classifica-

tion with self-supervised contrastive learning. In *Proceedings of the IEEE/CVF conference on computer vision and pattern recognition*, pages 14318–14328, 2021. [2](#), [5](#), [6](#)

[23] Hao Li, Ying Chen, Yifei Chen, Rongshan Yu, Wenxian Yang, Liansheng Wang, Bowen Ding, and Yuchen Han. Generalizable whole slide image classification with fine-grained visual-semantic interaction. In *Proceedings of the IEEE/CVF Conference on Computer Vision and Pattern Recognition*, pages 11398–11407, 2024. [1](#)

[24] Honglin Li, Yunlong Zhang, Pingyi Chen, Zhongyi Shui, Chenglu Zhu, and Lin Yang. Rethinking transformer for long contextual histopathology whole slide image analysis. *arXiv preprint arXiv:2410.14195*, 2024. [2](#)

[25] Ming Y Lu, Drew FK Williamson, Tiffany Y Chen, Richard J Chen, Matteo Barbieri, and Faisal Mahmood. Data-efficient and weakly supervised computational pathology on whole-slide images. *Nature biomedical engineering*, 5(6):555–570, 2021. [1](#), [5](#)

[26] Ming Y Lu, Bowen Chen, Drew FK Williamson, Richard J Chen, Ivy Liang, Tong Ding, Guillaume Jaume, Igor Odintsov, Long Phi Le, Georg Gerber, et al. A visual-language foundation model for computational pathology. *Nature Medicine*, 30(3):863–874, 2024. [2](#), [5](#), [6](#)

[27] Andrei Margeloiu, Matthew Ashman, Umang Bhatt, Yanzhi Chen, Mateja Jamnik, and Adrian Weller. Do concept bottleneck models learn as intended? *arXiv preprint arXiv:2105.04289*, 2021. [7](#)

[28] Pooya Mobadersany, Safoora Yousefi, Mohamed Amgad, David A Gutman, Jill S Barnholtz-Sloan, José E Velázquez Vega, Daniel J Brat, and Lee AD Cooper. Predicting cancer outcomes from histology and genomics using convolutional networks. *Proceedings of the National Academy of Sciences*, 115(13):E2970–E2979, 2018. [2](#)

[29] Andrew G Nicholson, Ming S Tsao, Mary Beth Beasley, Alain C Borczuk, Elisabeth Brambilla, Wendy A Cooper, Sanja Dacic, Deepali Jain, Keith M Kerr, Sylvie Lantuejoul, et al. The 2021 who classification of lung tumors: impact of advances since 2015. *Journal of Thoracic Oncology*, 17(3): 362–387, 2022. [7](#)

[30] Linhao Qu, Xiaoyuan Luo, Shaolei Liu, Manning Wang, and Zhijian Song. Dgmil: Distribution guided multiple instance learning for whole slide image classification. In *International Conference on Medical Image Computing and Computer-Assisted Intervention*, pages 24–34. Springer, 2022. [2](#)

[31] Ramprasaath R Selvaraju, Michael Cogswell, Abhishek Das, Ramakrishna Vedantam, Devi Parikh, and Dhruv Batra. Grad-cam: Visual explanations from deep networks via gradient-based localization. In *Proceedings of the IEEE international conference on computer vision*, pages 618–626, 2017. [2](#)

[32] Zhuchen Shao, Hao Bian, Yang Chen, Yifeng Wang, Jian Zhang, Xiangyang Ji, et al. Transmil: Transformer based correlated multiple instance learning for whole slide image classification. *Advances in neural information processing systems*, 34:2136–2147, 2021. [1](#), [2](#), [5](#), [6](#)

[33] Lloyd S Shapley et al. A value for n-person games. 1953. [7](#)

[34] Xiaoshuang Shi, Fuyong Xing, Yuanpu Xie, Zizhao Zhang, Lei Cui, and Lin Yang. Loss-based attention for deep multiple instance learning. In *Proceedings of the AAAI conference on artificial intelligence*, pages 5742–5749, 2020. [2](#)

[35] Andrew H Song, Richard J Chen, Tong Ding, Drew FK Williamson, Guillaume Jaume, and Faisal Mahmood. Morphological prototyping for unsupervised slide representation learning in computational pathology. In *Proceedings of the IEEE/CVF Conference on Computer Vision and Pattern Recognition*, pages 11566–11578, 2024. [1](#), [2](#), [5](#), [6](#)

[36] Susu Sun, Leslie Tessier, Frédérique Meeuwsen, Clément Grisi, Dominique van Midden, Geert Litjens, and Christian F Baumgartner. Label-free concept based multiple instance learning for gigapixel histopathology. *arXiv preprint arXiv:2501.02922*, 2025. [4](#)

[37] Yuxuan Sun, Yunlong Zhang, Yixuan Si, Chenglu Zhu, Zhongyi Shui, Kai Zhang, Jingxiong Li, Xingheng Lyu, Tao Lin, and Lin Yang. Pathgen-1.6 m: 1.6 million pathology image-text pairs generation through multi-agent collaboration. *arXiv preprint arXiv:2407.00203*, 2024. [2](#)

[38] Yonglong Tian, Dilip Krishnan, and Phillip Isola. Contrastive representation distillation. *arXiv preprint arXiv:1910.10699*, 2019. [6](#)

[39] Quoc Dang Vu, Kashif Rajpoot, Shan E Ahmed Raza, and Nasir Rajpoot. Handcrafted histological transformer (h2t): Unsupervised representation of whole slide images. *Medical image analysis*, 85:102743, 2023. [2](#)

[40] Hongyuan Wang, Fuyong Xing, Hai Su, Arnold Stromberg, and Lin Yang. Novel image markers for non-small cell lung cancer classification and survival prediction. *BMC bioinformatics*, 15:1–12, 2014. [2](#)

[41] Jia-Hong Wang, Ling-Feng Zhao, Hua-Feng Wang, Yue-Ting Wen, Kui-Kui Jiang, Xiang-Ming Mao, Zi-Ying Zhou, Kai-Tai Yao, Qing-Shan Geng, Dan Guo, et al. Genclip 3: mining human genes’ functions and regulatory networks from pubmed based on co-occurrences and natural language processing, 2020. [4](#)

[42] Yingxue Xu, Yihui Wang, Fengtao Zhou, Jiabo Ma, Shu Yang, Huangjing Lin, Xin Wang, Jiguang Wang, Li Liang, Anjia Han, et al. A multimodal knowledge-enhanced whole-slide pathology foundation model. *arXiv preprint arXiv:2407.15362*, 2024. [1](#)

[43] Zekang Yang, Hong Liu, and Xiangdong Wang. Scmil: Sparse context-aware multiple instance learning for predicting cancer survival probability distribution in whole slide images. In *International Conference on Medical Image Computing and Computer-Assisted Intervention*, pages 448–458. Springer, 2024. [2](#)

[44] Jiawen Yao, Sheng Wang, Xinliang Zhu, and Junzhou Huang. Imaging biomarker discovery for lung cancer survival prediction. In *Medical Image Computing and Computer-Assisted Intervention–MICCAI 2016: 19th International Conference, Athens, Greece, October 17–21, 2016, Proceedings, Part II 19*, pages 649–657. Springer, 2016. [2](#)

[45] Jiawen Yao, Xinliang Zhu, Jitendra Jonnagaddala, Nicholas Hawkins, and Junzhou Huang. Whole slide images based cancer survival prediction using attention guided deep multi-

ple instance learning networks. *Medical image analysis*, 65:101789, 2020. [5](#), [6](#)

[46] Jiawen Yao, Xinliang Zhu, Jitendra Jonnagaddala, Nicholas Hawkins, and Junzhou Huang. Whole slide images based cancer survival prediction using attention guided deep multiple instance learning networks. *Medical Image Analysis*, 65:101789, 2020. [2](#)

[47] Jin-Gang Yu, Zihao Wu, Yu Ming, Shule Deng, Yuanqing Li, Caifeng Ou, Chunjiang He, Baiye Wang, Pusheng Zhang, and Yu Wang. Prototypical multiple instance learning for predicting lymph node metastasis of breast cancer from whole-slide pathological images. *Medical Image Analysis*, 85:102748, 2023. [2](#)

[48] Neda Zamanitajeddin, Mostafa Jahanifar, and Nasir Rajpoot. Cells are actors: Social network analysis with classical ml for sota histology image classification. In *Medical Image Computing and Computer Assisted Intervention–MICCAI 2021: 24th International Conference, Strasbourg, France, September 27–October 1, 2021, Proceedings, Part VIII* 24, pages 288–298. Springer, 2021. [2](#)

[49] Sheng Zhang, Yanbo Xu, Naoto Usuyama, Hanwen Xu, Jaspreet Bagga, Robert Tinn, Sam Preston, Rajesh Rao, Mu Wei, Naveen Valluri, et al. Biomedclip: a multimodal biomedical foundation model pretrained from fifteen million scientific image-text pairs. *arXiv preprint arXiv:2303.00915*, 2023. [2](#)

[50] Xinmin Zhang. Molecular classification of breast cancer: Relevance and challenges. *Archives of Pathology & Laboratory Medicine*, 147(1):46–51, 2023. [4](#)

[51] Yi Zheng, Rushin H Gindra, Emily J Green, Eric J Burks, Margrit Betke, Jennifer E Beane, and Vijaya B Kolachalam. A graph-transformer for whole slide image classification. *IEEE transactions on medical imaging*, 41(11):3003–3015, 2022. [2](#)

[52] Xinliang Zhu, Jiawen Yao, and Junzhou Huang. Deep convolutional neural network for survival analysis with pathological images. In *2016 IEEE international conference on bioinformatics and biomedicine (BIBM)*, pages 544–547. IEEE, 2016. [2](#)

APPENDIX

A. Dataset

NSCLC: For the No-Small Cell Lung Carcinoma (NSCLC) subtyping task, we use the Hematoxylin and Eosin (H&E) Formalin-Fixed and Paraffin-Embedded (FFPE) WSIs from TCGA and CPTAC. Both TCGA and CPTAC cohorts contain two subtypes: lung adenocarcinoma (LUAD) and lung squamous cell carcinoma (LUSC). The TCGA cohort contains a total of 1033 slides (LUAD: 523, LUSC: 510) and the CPTAC cohort contains a total of 1372 slides (LUAD: 683, LUSC: 689).

RCC: For the Renal Cell Carcinoma (RCC) subtyping, we use the H&E-stained FFPE WSIs from TCGA and CPTAC. The TCGA cohort contains three subtypes: Clear Cell Renal Cell Carcinoma (CCRCC), Papillary Renal Cell Carcinoma (PRCC), and Chromophobe Renal Cell Carcinoma (CHRCC). The CPTAC cohort contains two subtypes: CCRCC and PRCC. The TCGA cohort contains a total of 873 slides (CCRCC: 506, PRCC: 271, CHRCC: 66). The CPTAC cohort contains a total of 555 slides (CCRCC: 524, PRCC: 31).

B. Additional Experiment Results

Experiment results of GP-NN. Table B.1 presents the experimental results of GP-NN for NSCLC subtyping and RCC subtyping based on transcriptomics data. Transcriptomic data typically contain more distinctive biomarkers for differentiating cancer subtypes, and neural networks often achieve better performance in subtype classification when utilizing transcriptomic data. From Table 1, it can be observed that PA-MIL, based on WSI data, achieves better performance in RCC subtyping.

Table B.1. Experiment Results of GP-NN.

Method	NSCLC		RCC	
	Acc.	AUC	Bal acc.	F1
GP-NN(RNA-Seq)	97.19±1.53	98.82±0.64	95.13±1.07	95.59±1.26
PA-MIL(WSI)	94.68±1.30	98.42±0.84	95.66±1.86	95.69±0.59

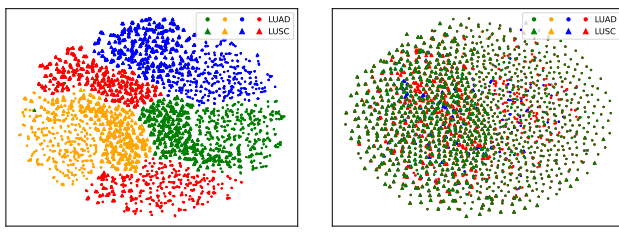


Figure B.1. Distribution of phenotype features.

Ablation of phenotype features alignment (PA). PA-MIL learns subtype-agnostic, mutually independent phenotypic features, enabling a concise and scalable solution for diverse cancer tasks. The primary goal of PA is to constrain phenotypic features, enhancing the reliability of model interpretation. Figure B.1a and Figure B.1b show the distribution of features corresponding to the top-4 contributing phenotypes in the feature space, with PA enabled and disabled, respectively. As shown, in the absence of PA, the features are randomly scattered. In contrast, with PA enabled, the phenotypes form clearly distinct distributions.

C. Phenotype Knowledge Base

Table C.2 and Table C.3 respectively present the phenotypic knowledge bases we have constructed for NSCLC and RCC. The phenotypic knowledge base for NSCLC contains 17 phenotypes, while the phenotypic knowledge base for RCC contains 16 phenotypes. Each phenotype includes its morphological description and potentially associated genes.

Table C.2. Phenotype knowledge base of NSCLC.

Phenotype name	Morphological description	Associated gene sets
Glandular Formation	The presence of gland-like structures lined by malignant cells that may produce mucus. These glandular patterns can appear as circular or irregular formations, often with luminal spaces containing mucus.	APC, MUC5AC, PTGS2, TP53, CTNNB1, KLK4, GHRH, PRL, ESR1, POMC, PTEN, FOXA2, EGFR, CD44, AKT1, MUC1, GAL, KRAS, MEN1, SOX9, PPARD, MAPK1, KCNJ5, VIM, AIP, CDH1, GHR, IGF1, MAP2K7, MYC, LGR5, PPARA, LIF, EZH2, IL6, CCND1, ARHGEF4, NFE2L2, FOXP3, KIT, AGER, CDK4, PAX8, BCL2, POU1F1, SPARC, FGF10, GJA1, CYP19A1, CLDN1
Mucin Production	Cells within the tumor may contain intracytoplasmic mucus, which can be visualized as vacuoles inside the cells with special stains like mucicarmine or PAS with diastase.	MUC5AC, IL13, MUC2, EGFR, IL4, IL5, CFTR, MUC5B, ANO1, MUC1, TAC1, MUC3A, CXCL8, IL17A, VIP, MAPK1, CLCA1, GAST, IL10, TNF, IFNG, STAT6, SCT, TGFA, MPO, CALCA, ALB, TJP1, IL6, ALK, PTGS2, NOS2, OCLN, ELANE, HAVCR2, F2RL1, CDX2, IL1B, IGHE, LEP, CCL11, PTGER4, MUC4, CD79A, PTGER3, MMP9, CDH1, GCG, TLR4, IL22
Lepidic Growth	Flattened or slightly atypical cells growing along pre-existing alveolar structures without invasion into the surrounding lung parenchyma. This pattern gives a paving stone appearance and is often seen in the early stages of adenocarcinoma in situ.	EGFR, SERPINB3, MUC5AC, ALK, PDPN, TP63, CD274, VEGFA, CDH1, KRAS, NKX2-1
Acinar Formation	This pattern consists of round or ovoid acini or tubules made up of neoplastic cells, resembling normal lung acinar structures.	KRAS, EGFR, CCK, AQP5, MUC5AC, ALK, TAC1, BHLHA15, CDH1, CD274, TNF, SOX9, TP53, MMP9, GCG, BCL2L11, FCGRT, TP63, VIP, NR5A2, SST, GRP, SNAI1, MAP1LC3A, PDX1, MUC1, PIK3CA, TLR3, NEUROG3, SMARCA4, VMP1, RHOA, VAMP2, APC, MAPK1, KIT, KRT19, CDK2, GRB2, CD34, MYC, KRT7, SCT, CXCL2, CTNNB1, BRAF, AQP3, STAT3, GPX4, TIMP1
Papillary Structures	The presence of finger-like projections lined by neoplastic cells with or without fibrovascular cores. These projections can be complex and branching.	MUC5AC, CALCA, BDNF, GNAT3, TAC1, CD36, SHH, TAS1R3, UCHL1, TCHH, SOX2, TAS1R2, TAS2R38, TAS1R1, BMP2, ENO2, TP53, IGF1, AVP, TRPV1, FFAR4, BRAF, EGFR, KRT7, ACHE, NTRK2, VIM, TP63, BMP4, TGFB1, CD34, ACE2, KRT14, NGFR, AQP2, SNAP25, MME, GAL, CD79A, NPY, LGR5, SPP1, NTF3, NCAM1, GLI1, SST, FGF2, FST, FLG, MKI67
Micropapillary Features	Small papillary tufts lacking a fibrovascular core, often appearing as free-floating within alveolar spaces, and associated with high-grade tumors and poor prognosis.	EGFR, ERBB2, TP53, MUC1, MUC5AC, ALK, CDH1, NKX2-1, CD274, TP63, BRAF, WT1, KRT7, MME, PAX8, SMARCA2, KRAS, MET

Continued on next page

Table C.2 – continued from previous page

Phenotype name	Morphological description	Associated gene sets
Solid Growth Pattern	Sheets or nests of cells with little or no glandular or acinar differentiation. There can be high cellularity, and necrosis may be present.	EGFR, ALK, TP53, MUC5AC, RET, CDH1, KRAS, ACCS, PTGS2, PCNA, MKI67, TG, VEGFA, KIT
Stromal Invasion	Invasive adenocarcinoma is characterized by the neoplastic cells breaching the basement membrane and infiltrating into the surrounding stroma, with possible desmoplastic reaction.	MMP9, AKT1, CDH1, MMP2, ERBB2, VEGFA, EGFR, TP53, MAPK1, STAT3, HGF, CXCR4, CD44, SNAI1, VIM, PTGS2, MMP14, MET, PTK2, PGR, PIK3CA, TGFB1, IL6, PTEN, AFP, MTOR, CXCL12, MAPK3, ZEB1, CDH2, PLAUR, SRC, PLAUR, CD274, MYC, TWIST1, BCL2, HPSE, RAC1, EZH2, RHOA, BSG, CCND1, MMP7, MMP1, CXCL8, YAP1, NFKB1, CTNNB1, BRAF
Tumor Stroma	A variable amount of connective tissue can accompany the tumor cells, ranging from a scant fibrous stroma to dense fibrosis, which is commonly seen in the scarred or fibrotic focus of the tumor.	CD274, PDCD1, VEGFA, CD8A, IL6, EGFR, STAT3, FOXP3, TP53, IDO1, IL10, CXCR4, CD4, CCL2, ERBB2, CTLA4, TGFB1, FAP, CXCL12, METTL3, CD68, PTGS2, AKT1, MMP9, MMP2, CD163, CXCL8, TNF, IL17A, IL2, KRAS, NTSE, CD44, HIF1A, MTOR, HGF, CAV1, IFNG, MYC, HAVCR2, CCL5, CD47, VIM, POSTN, PIK3CA, PTEN, SPARC, CSF2, MUC5AC, SPP1
Lymphovascular Invasion	Tumor cells may be seen within lymphatic or blood vessels, suggesting a mechanism for potential metastasis.	VEGFA, ERBB2, TP53, AFP, PGR, MMP9, CDH1, EGFR, CD274, MMP2, ALB, BCL2, PTGS2, BRAF, MUC5AC, PDPN, PECAM1, CD34, CEACAM5, CCND1, SERPINB3, KRAS, KDR, CRP, CD44, AKT1, VEGFC, NODAL, BIRC5, CDKN2A, MKI67, COX8A, PCNA, HIF1A, MUC1, FGF2, PROM1, VIM, CXCR4, MET, CTNNB1, PTEN, PIK3CA, MUC16, FLT1, IL6, NFKB1, LGALS3, VEGFD, SPP1
Adenocarcinoma Cell	The lung adenocarcinoma cells include pleomorphism of the nucleus with varying sizes, high nuclear to cytoplasmic ratio, active nuclear division, abundant cytoplasm, commonly exhibiting glandular structures, tight cell arrangement, and minimal intercellular stroma.	SERPINB3, EGFR, TP53, CD274, MUC5AC, KRAS, ALK, ERBB2, AKT1, CDH1, MALAT1, TP63, PTGS2, CDKN2A, PDCD1, NKX2-1, VEGFA, MAPK1, BCL2, MUC1, CD44, CEACAM5, TGFB1, ABCB1, EPCAM, PCNA, MYC, CCND1, IFNG, CDKN1A, TNF, STAT3, CASP3, IL6, PIK3CA, NFKB1, TNFSF10, PROM1, MTOR, ENO2, KRT5, MET, MMP9, BIRC5, BRAF, BAX, MMP2, VIM, CD8A, PTEN

Continued on next page

Table C.2 – continued from previous page

Phenotype name	Morphological description	Associated gene sets
Keratinization	Keratinization is indicated by the presence of orangeophilic (eosinophilic), dense, lamellar keratin within cancer cells or as keratin pearls. Keratin pearls are formed when concentric layers of squamous cells undergo keratinization resulting in a whorled appearance.	FLG, IVL, KRT10, SERPINB3, TGM1, KRT1, CASP14, TP53, TCHH, KRT14, MUC5AC, KRT16, SPRR1B, KRT13, HRNR, CDKN2A, KRT19, EGFR, STS, KRT17, TGM3, BCL2, GJB2, CDSN, NFE2L2, OMA1, CST6, KRT5, GJB4, KLK7, FGF7, ABCA12, CD8A, MMP9, VIM, KRT2, PRL, LPA, NUTM1, GJA1, KLRD1, HSPB1, CD4, CLU, IL17A, ATP2A2, IL2, KLRB1, GJB3, CTNNB1
Intercellular Bridges	Also known as desmosomes, intercellular bridges appear as small lines or tiny spicules joining adjacent tumor cells. They are best viewed at high magnification and are indicative of squamous differentiation.	GJA1, GJD2, GJB1, GJB2, GJA5, GJC1, GJB6, GJA8, GJA4, PANX1, TJP1, GJA3, CDH2, CDH1, GJC2, SRC, OCLN, MAPK1, EMILIN1, MIP, REN, TEX14, PVALB, DSP, AKT1, GJB3, VEGFA, OXT, EDN1, TNF, AGT, CDH5, AQP4, KNG1, IGF1, MAPK8, CTNNB1, CGA, IL1B, VIM, PRKCG, SCN5A, KCNA3, KIT, GFAP, GJB4, GNRH1, NEUROD1, DES, MAPK3
Squamous Cell Carcinoma Cell	Squamous cell carcinoma cells are often polygonal in shape and show varying degrees of atypia, including large hyperchromatic nuclei, prominent nucleoli, and irregular nuclear contours. The cytoplasm can range from scant to eosinophilic and dense, sometimes with clear perinuclear halos.	SERPINB3, EGFR, TP53, CDKN2A, CD274, AKT1, VEGFA, PDCD1, CCND1, CDH1, TP63, PTGS2, STAT3, BCL2, PIK3CA, ERBB2, CD44, BIRC5, CEACAM5, MMP9, IL6, KRT19, MTOR, MAPK1, MYC, CDKN1A, ENO2, PTEN, SOX2, MMP2, PDPN, NODAL, ALB, PCNA, MET, DNAJB7, CXCR4, VIM, YAP1, IL2, CASP3, CXCL8, MUC1, CD8A, CRP, KRAS, CTNNB1, NOTCH1, NFE2L2, TGFB1
Necrosis	Necrosis can often be seen as areas of more eosinophilic staining where the tissue architecture is lost. Geographic necrosis, where large areas necrose in a map-like pattern, may be present.	TNF, IL6, IL1B, IL10, IFNG, CRP, CXCL8, CCL2, IL2, IL4, TNFSF10, NFKB1, PTGS2, IL17A, NOS2, VEGFA, ICAM1, CASP3, CSF2, IL1A, MPO, ADIPOQ, LEP, TNFRSF1A, FAS, TLR4, TGFB1, SOD1, BCL2, IL18, TNFRSF1B, GPT, VCAM1, MMP9, IL5, CAT, IL1RN, IL13, RELA, TP53, LTA, MAPK1, MAPK14, BAX, HMGB1, FASLG, MAPK8, IFNA1, AKT1, LPA
Inflammatory Infiltrate	A variable amount of inflammatory cells, including lymphocytes and macrophages, can commonly be found infiltrating the tumor stroma, sometimes obscuring the tumor cells.	TNF, CD68, CD4, ICAM1, IFNG, CD8A, CCL2, IL10, IL17A, MPO, IL4, VEGFA, FOXP3, MUC5AC, IL1B, PTGS2, IL6, IL5, TGFB1, IL2, NOS2, MMP9, VCAM1, PTPRC, BCL2, NFKB1, CCL5, IL13, CASP3, CSF2, CD1A, TNFRSF8, MS4A1, CD34, ITGAM, PRF1, CD274, FASLG, TP53, GZMB, PDCD1, TLR4, CXCL2, IGHE, PECAM1, CXCL1, MPV17, ITGAX, KIT, ELN

Continued on next page

Table C.2 – continued from previous page

Phenotype name	Morphological description	Associated gene sets
Mitotic Figures	Mitotic figures indicate cellular division. These figures can appear as dark, dense, thread-like structures within the nucleus of cells undergoing mitosis.	TP53, MKI67, PCNA, MUC5AC, KIT, CD34, BCL2, CDKN2A, VIM, GFAP, DES, EGFR, BRAF, SYP, BRCA1, CCND1, CDKN1A, VEGFA, IDH1, BIRC5, ENO2, MAD2L1, CDK1, ALK, MYC, CD99, KRT7, CDH1, KRT19, ERBB2, EZH2, TP63, PECAM1, SERPINB3, TERT, CSF3, PRL, ALB, CASP3, SST, IGF1, CHGA, EPO, CCL4, IL2, TOP2A, ANO1, MLANA, BAP1, CTNNB1

Table C.3. Phenotype knowledge base of RCC.

Phenotype name	Morphological description	Associated gene sets
Clear Cytoplasm	Tumor cells have a clear or vacuolated cytoplasm due to the accumulation of lipids or glycogen, presenting as pale or unstained cytoplasm.	MUC5AC, MME, VIM, AFP, KRT7, TFE3, MLANA, KIT, TP53, CD68, EWSR1, SALL4, BCL2, GPC3, DES, GFAP, PLIN2, CALCA, CA9, KRT20, HSPA4, NCAM1, MS4A1, MUC1, PRCC, TP63, POU5F1, SDHB, TFEB, NR5A1, TAC1, KRT8, TGFB1, CDX2, TJP2, SPOP, SERPINB3, VHL, ELOC, TJP1, ENO2, CDKN2A, HMGB1, CTNNB1, SYP
Eosinophilic Cytoplasm	The cytoplasm is more granular and exhibits eosinophilia, typically appearing pale pink or brown due to the presence of a higher number of mitochondria and other organelles within the cell.	MUC5AC, VIM, CD68, DES, KIT, TFE3, SYP, PRCC, ENO2, KRT7, AFP, KRT20, CD163, SOX10, MB, S100B, CD34, CALB2, MLANA, CDKN2A, CHGA, TP63, ALK, BAP1, SDHB, SMARCB1, CD99, EWSR1, BRAF, CASP3, SPN, MPO, GPC3, EPX, WT1, MUC1, GFAP, TNFRSF8, CLC, GATA3, RNASE3, MS4A1, AMACR, PIP, TP53, SETD2, PECAM1, EGFR, CDH1, SST
Papillary Structure	The cancer tissue shows typical papillary structures, with a central vascular core, and cells arranged in clusters or layers, with broad bases.	MUC5AC, RET, PTCH1, BRAF, TPCN1, VEGFA, TG, CDH1, CD34, KRAS, FGFR3, NTRK1, PECAM1, SPP1, ESR1, KNG1, TP63, CCDC6, EFEMP1, EGFR, SHCBP1
Capsular Invasion	Tumor cells may invade through the renal capsule, extending into the perirenal fat tissue, leading to an ill-defined tumor margin.	BRAF, AFP, TP53, TG, VEGFA, ALB, CALCA, KRT19, COX8A, CDH1, RET, PTEN, CD274, ERBB2, CTNNB1, TERT, MMP2, CCND1, LGALS3, KRT7, BCL2, EGFR, PTGS2, TPO, CASP3, SLC2A5, CCDC6, TSHR, TIMP2, HIF1A, MUC5AC, PPARG, PCNA, FOLH1, PTH, GPT, HSPA4, CD44, MKI67, NOTCH1, EBAG9, CRP, MDM2, NODAL, MME, ALPP, CEACAM5, CD34, VHL, AGGF1

Continued on next page

Table C.3 – continued from previous page

Phenotype name	Morphological description	Associated gene sets
Vascular Proliferation	The tumor exhibits numerous irregular blood vessels with thin walls, often showing areas of hemorrhage or thrombus, creating a vascular network appearance.	VEGFA, KDR, FGF2, AKT1, PECAM1, HIF1A, PTGS2, MAPK1, MMP9, EGFR, FLT1, TP53, ANGPT2, COL18A1, STAT3, THBS1, CD34, ANGPT1, MTOR, IL6, CXCL8, TEK, TGFB1, HGF, MMP2, CXCL12, PIK3CA, ENG, CXCR4, PGF, NOS3, AGT, BCL2, MAPK3, CCL2, TNF, IGF1, SERPINF1, ANG, NRP1, NFKB1, HPSE, EPO, LEP, CDH5, ERBB2, SPP1, CASP3, MYC, DLL4
Large and Irregular Nuclei	Cancer cells have large, irregularly shaped nuclei, often with prominent nucleoli.	THPO, IL3, CD34, MPL, CSF2, KITLG, IL6, GATA1, ITGA2B, EPO, PF4, CSF3, IL11, ITGB3, MSLN, PTPN4, NFE2, FLT3, JAK2, RUNX1, ACHE, TGFB1, GP1BA, FLI1, AKT1, GATA2, KIT, MAPK1, ZFPM1, GP6, TIMP1, PPBP, SPI1, CXCL12, PTPN11, TAL1, CALR, MYB, TP53, CXCR4, IL1B, BCL2L1, GFI1B, FLT3LG, SPP1, PRG4, ALB, IFNA1, KLF1, CASP3
Capillary Network	A rich capillary network is often observed within the tumor, particularly surrounding the papillary structures.	VEGFA, EDN1, ALB, AGT, TNF, NOS3, ICAM1, KNG1, KANTR, PECAM1, REN, NOS2, CALCA, LPA, CD34, ACE, KDR, ADAMTS13, IL6, EGR3, SERPINC1, PLAT, HMOX1, PROC, VCAM1, SOD1, PTGS2, AKT1, AVP, IL2, GAST, SST, FGF2, VIP, ANGPT1, GCG, MPO, SDC1, EPO, THBD, NPY, KLK4, ADIPOQ, ITGB2, TAC1, IGF1, NOS1, HIF1A, TGFB1, EDNRA
Nuclear-to-Cytoplasm Ratio	The nuclei occupy a smaller proportion of the cell volume, with relatively abundant cytoplasm.	CRP, ALB, LPA, MAPK8, CST3, IL6, BAX, CASP3, BCL2, MAPK1, JUN, NAGLU, APOA1, GDF15, PPP1R1A, APOB, PROC, TNF, AKT1, MAPK3, EAF2, ABCG2, BGLAP, TP63, MET, CYP2C19, NPPB, LCN2, PROS1, MAPK14, RBP4, CASP9, REN, LEP, ADIPOQ, CAT, MPO, EGFR, MTOR, RELA, TF, TP53, IGF1, GPT, SOD1, TLR4, CYP2D6, SERPINC1, IL10, PARP1
Glandular Structure	Some tumors exhibit glandular patterns, with tubular or acinar arrangements of cells.	MUC5AC, KLK4, KLK2, CDH1, REN, CEA-CAM5, LIF, GAST, PTGS2, VIM, CD44, ADIPOQ, PTH

Continued on next page

Table C.3 – continued from previous page

Phenotype name	Morphological description	Associated gene sets
Inflammatory Infiltrate	A variable amount of inflammatory cells, including lymphocytes and macrophages, can commonly be found infiltrating the tumor stroma, sometimes obscuring the tumor cells.	CCL2, TNF, IL10, MPO, IL17A, IL4, CD68, IL6, ICAM1, CD4, IL13, PTGS2, VEGFA, IFNG, CD8A, TLR4, IL5, NLRP3, IL1B, MMP9, NOS2, MUC5AC, PTPRC, VCAM1, FOXP3, IL2, BCL2, SOD1, NFKB1, TGFB1, CXCL2, CCL5, ALB, RELA, IL18, CASP3, HMGB1, CD274, PECAM1, CSF2, GPT, STAT3, MAPK1, MYD88, PDCD1, IL23A, CASP1, CAT, AKT1, CD34
Vascular Endothelial Proliferation	The presence of numerous small, thin-walled blood vessels interspersed among tumor cells, forming a network-like pattern.	VEGFA, KDR, FGF2, AKT1, PECAM1, HIF1A, PTGS2, MMP9, EGFR, FLT1, ANGPT2, COL18A1, MAPK1, TP53, THBS1, STAT3, CD34, ANGPT1, MTOR, IL6, CXCL8, TEK, HGF, TGFB1, MMP2, CXCL12, ENG, PIK3CA, CXCR4, NOS3, PGF, BCL2, CCL2, TNF, MAPK3, SERPINF1, IGF1, ANG, NRP1, HPSE, EPO, NFKB1, LEP, CDH5, DLL4, CASP3, ERBB2, MET, SPP1, MYC
Granular Cell Type	Cells containing abundant eosinophilic granules in the cytoplasm, resulting in a granular appearance.	FCGR3A, NCAM1, ENO2, B3GAT1, VIM, PRF1, CD8A, CALB2, TIA1, MS4A1, CD2, TGFB1, FOS, STAT3, GFAP, CD68, CCK, IL2, MUC1
Necrosis	Areas within the tumor exhibiting necrotic tissue, appearing as irregular, acellular regions.	TNF, IL6, IL1B, IL10, IFNG, PDCD1, CASP3, CD274, CRP, BCL2, TP53, IL2, CXCL8, CCL2, IL4, FAS, TNFSF10, NFKB1, BAX, PTGS2, VEGFA, IL17A, NOS2, AKT1, MAPK1, ICAM1, CSF2, MAPK8, SOD1, MPO, FASLG, ADIPOQ, IL1A, TNFRSF1A, CASP8, TLR4, LEP, TGFB1, IL18, PARP1, MAPK14, CAT, ANXA5, CASP1, CTLA4, TNFRSF1B, HMGB1, GPT, VCAM1, MMP9
Fibrous Stroma	Presence of dense fibrous tissue within the tumor, often surrounding blood vessels or tumor nests.	CD34, MUC5AC, KRT19, TGFB1, ELN, KRT7, CD44, CD68, VEGFA, VIM, MME, EPCAM, S100A4, SYP, CDH1, DES, CD274, GFAP, DCN, FGF2, TNFSF11, MUC1, FAP, NES, MFAP5, STAB1, PDGFRB, PGR, SALL4, CDKN2A, THBS1, TP53, LOXL2, PECAM1, PDCD1, MMP2, CD4, MKI67, FGF7, CALCA, DPP4, TIMP1, F13A1, UCHL1

Continued on next page

Table C.3 – continued from previous page

Phenotype name	Morphological description	Associated gene sets
Mitotic Activity	The presence of numerous mitotic figures, indicating active cell division, with visible separation of nuclear and cytoplasmic components.	TP53, CDK1, PCNA, MKI67, KIT, PLK1, BCL2, ERBB2, CCNB1, PGR, CD34, VEGFA, WEE1, CDKN2A, VIM, CDC25C, PTPA, CDKN1A, KIF11, CCND1, CDC20, EGFR, AURKA, CDC14A, CASP3, MYC, CAT, MUC5AC, CDH1, TTK, BUB1B, MAPK1, MAD2L1, BIRC5, PTGS2, PRL, FGF2, IGF1, TOP2A, FZR1, CDK2, AKT1, APC, AURKB, IL6, BRCA1, MTOR, BRAF, ALB, KIF2C
Calcification	Focal calcification within the tumor, which appears as basophilic or eosinophilic deposits, often seen as small granular or block-like structures.	BGLAP, RUNX2, SPP1, ALPP, BMP2, PTH, MGP, TNFRSF11B, FGF23, IBSP, AHSG, SP7, LPA, ALPL, DMP1, DSPP, ENPP1, ELN, TNFSF11, KL, MAPK1, CRP, ABCC6, SOST, SPARC, AKT1, ALB, VDR, PHEX, SLC20A2, VEGFA, IGF1, TGFB1, IL6, COL1A1, FGF2, CCL27, BMP7, BMP4, LEP, AMELX, MAPK3, SOX9, GDF2, CALCA, MSX2, ANKH, MAPK14, APOE, TNF